Light scattering model for small space debris particles

Peltoniemi, Jouni I.

2022-11-15

Light scattering model for small space debris particles

Jouni I. Peltoniemi [a,*], Nataliya Zubko [a], Anne K. Virkki [a,d], Maria Gritsevich [a]
Jarmo Moilanen [a], Jean-Christophe Roulet [b], David Nguyen [b], Valentin Mitev [b],
Robin Putzar [c], Erkai Watson [c], Martin Schimmerohn [c], Antti Penttilä [d],
Karri Muinonen [d], Mark Millinger [e]

[a] *Finnish Geospatial Research Institute FGI, Vuorimiehentie 5, Espoo 02150, Finland*
[b] *CSEM, Centre Suisse d'Electronique et de Microtechnique SA, Jaquet–Droz 1, Neuchâtel CH-2002, Switzerland*
[c] *Fraunhofer-Institute for High-Speed Dynamics, Ernst-Mach-Institut, EMI, E.-Zermelo-Str. 4, 79104 Freiburg, Germany*
[d] *Department of Physics, P.O. Box 64, University of Helsinki, 00014, Finland*
[e] *ESA, ESTEC, Keplerlaan 1, AZ Noordwijk 2201, the Netherlands*

Abstract

We have developed a scattering model allowing to study interaction of light with particles populating the near-Earth environment: satellite explosion remnants, collisional debris, particles detached from peeling paint surfaces, and ejecta resulting from micrometeorite bombardment. In its present configuration the model accounts for rough needles, grains, and plates as primary shape elements. More complex shapes are built upon combining them.

The model is compared and validated against laboratory measurements. The studied samples include a set of space debris analogue samples obtained from the controlled MIRAD (Microparticle impact related attitude disturbances) experiment that collided solar cell panels with a projectile. The resulting samples are mostly carbon needles and curved aluminium sheets. We have both measured and modelled the scattering of light from a set of these samples.

The model agrees rather well with the measurements. The shape and orientation of the particles are found to be the main contributor in how light is scattered, whereas the material dependence shows a weaker trend. Large amount of data with varying viewing and illumination angles are needed to allow for inversion of the target characteristics.

The experimental results exploited in our study have significantly aided the model development. In the future, this work can be expanded to a real-mode in-orbit scattering model that can be utilised in Earth system and/or astronomical observations and space mission concept designs. Additional measurements with larger variety of samples and their expanded size range are required to extend and solidify the model for the full range of populations representing space particles.

1. Introduction

Near-Earth space is getting crowded. According to the space debris statistics of the European Space Agency (ESA), the number of launched payloads increased from about 400 per year in 2017–2019 to more than 1750 in 2021 in the Low-Earth Orbit (LEO, perigee < 2,000 km) alone, because of the increase in especially commercial operators and applications. The number of re-entries has remained in a few hundred per year, so the number of catalogued payload- and rocket-related objects and debris

---

* Corresponding author.
E-mail address: jouni.peltoniemi@nls.fi (J.I. Peltoniemi).

Table 1
Abundance, available tracking data, and typical effects of space debris in Earth orbit for five different size ranges. (Schimmerohn et al., 2018).

Size range	Amount	Data source	Effect on a satellite
> 10 cm	∼37 000	tracked using telescopes, radars, lasers	catastrophic collision; the target disintegrates into numerous smaller and larger particles; fragment sizes depend on impactor size and collision scenario
1–10 cm	1 million	only few random observations	termination of mission; significant amount of new debris is created
1–10 mm	> 300 million	no tracking data	penetration of typical spacecraft structure walls; subsystem malfunction or termination of mission, depending on impact location
0.1–1 mm		some impact marks observed	damages sensitive parts, leaves visible marks
< 0.1 mm		collectors in spacecrafts	drag and wear; degradation of optical surfaces (windows, solar cells)

orbiting the Earth has now increased to more than 18,000 in LEO and to more than 36,600 in total. In addition, the number of uncatalogued fragments of debris, originating from various accidental or deliberate collisions and issues related to electronics, aerodynamics and propulsion, is estimated at more than 130 million[1] (Pardini and Anselmo, 2011; ESA, 2022).

The population of larger, about 10 cm and up, space debris is known and monitored, and collision risks can be evaluated and several avoidance manoeuvres are performed annually. However, the increasing number of objects poses an increasing threat to the satellite operations. A non-negligible probability for collisions exists, which may lead to more debris, more collisions, and very large costs. In fact, ESA's Space Debris Office reports the number of fragmentation events at approximately ten per year, and the cost of monitoring of possible collisions and the avoidance manoeuvring at millions of euros. The data are collected in DISCOS database (Database and Information System Characterising Objects in Space) (Torre et al., 2001; Flohrer et al., 2013; DISCOS, 2022), and MASTER (ESA Meteoroid and Space Debris Terrestrial Environment Reference model) provides model for full population Flegel et al. (2009), MASTER (2022), using e.g. fragmentation modelling Fragmentation database (2022).

Table 1 lists the estimated abundance of space debris particles in five different size categories, available tracking data for them, and their typical effects on a target when impacting. As shown in the table, only random observations of 1–10-cm particles exist, and nothing in the 0.1–10-mm range. Observations of objects smaller than 0.1 mm are collected by impact detectors.

New observational methods are needed for improved tracking of space objects especially in the size categories from 1 mm to 10 cm. One possibility is to use dedicated space-based sensors. An orbital detector would hold considerable advantage over ground-based techniques, would provide a wide coverage, and would escape dependency on weather conditions (Bouquet et al., 2014). Even a rather small detector could observe objects in short distances.

Currently, there is at least one in orbit sensor, the Canadian NEOSSAT (Near Earth Object Surveillance Satellite) (Abbasi et al., 2019; Laurin et al., 2008),

Following recommendations of (Englert et al., 2014; Worms et al., 1999), ESA has recently started the project on developing Coincident laser sheet particle monitor (COLA), to study the feasibility of a new orbital sensor (Peltoniemi et al., 2021). The idea is based on placing one or more thin laser sheet light fields around the satellite, and several fast cameras measuring the precise coordinates and brightness of the flashes caused by bypassing particles. These measurements can be used to retrieve the trajectory and physical properties of the particles. The aim of the present work is to research on the physical signals the debris particles in laser light could make to a sensor.

2. Particles in the scattered light

In a typical setup, we have a light source (Sun, laser, etc) producing a beam at direction $\hat{\mathbf{k}}_0$ and intensity I_0 at the target, and a sensor at direction $\hat{\mathbf{k}}_s$ and distance $\mathbf{r}$ from the scatterer (Fig. 1). The scattered irradiance I_s [W/m^2] at the sensor can be then given as

$$I_s(\hat{\mathbf{k}}_s) = \frac{1}{\mathbf{r}^2} \frac{a(\iota, \xi) P(\alpha, \phi, \iota, \xi)}{4\pi} A(\iota, \xi) I_0(\hat{\mathbf{k}}_0) \qquad (1)$$

where α is the phase angle, ϕ is the azimuth scattering angle, ι is the angle between the particle main axis (most symmetric axis) $\hat{\mathbf{n}}$ and incident direction $\hat{\mathbf{k}}_0$, ξ is the particle rotation phase around the main axis, [geometric] cross-section is A, [Bond] albedo is a, and P is the [scattering] phase function. Typically, we have several observations of the target with varying distance and/or angles. To be able to analyse the observation data, we need a model for the phase function, albedo, and cross-section.

There are already numerous scattering models for planetary, atmospheric, soil particles (Bohren and Huffman, 1983; Mishchenko et al., 2000; Muinonen et al., 2019; van de Hulst, 1957), and many more. Some of them are validated with novel reflectance measurements, for example, with a help of the acoustic waves (Maconi et al., 2020; Maconi et al., 2018; Helander et al., 2020).
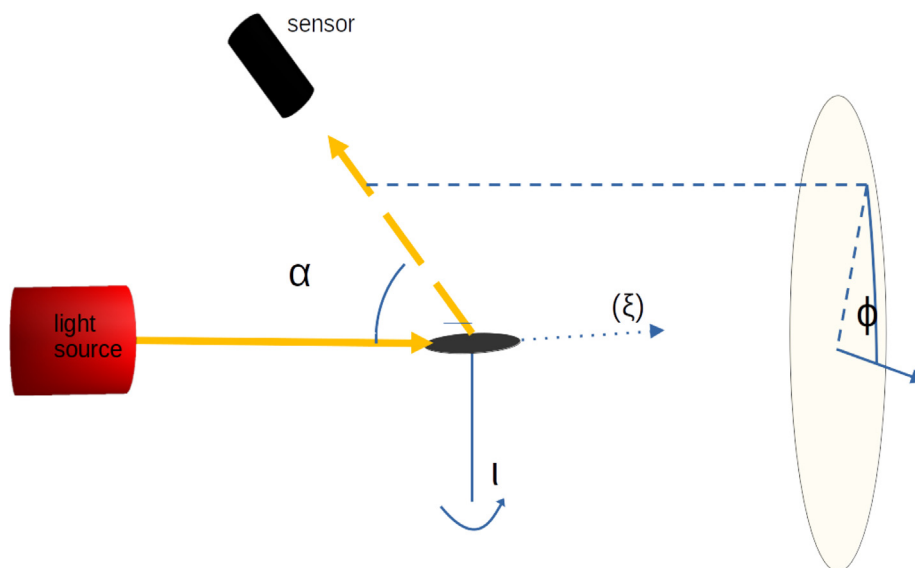
Fig. 1. The model and measurement geometry. The light source illuminates from left. The sensor moves around the target, with a phase angle α and azimuth ϕ, measured from horizontal. The target's main axis is rotated along a vertical axis an angle $\imath$ from the beam direction. The last rotation angle ξ of the particle is not used here.

However, anthropogenic space particles differ significantly from these, and new scattering models are needed. We can assume MASTER (Flegel et al., 2009; MASTER, 2022) and ORDEM (NASA's Orbital Debris Engineering Model) (Krisko et al., 2015) to provide up-to-date (though still limited) knowledge on particle sources and distributions. We can collect information on recent experiments on particle shapes and properties (Allen and Fitz-Coy, 2020; Krisko et al., 2008; Watson et al., 2020; Cowardin et al., 2020; Akahoshi et al., 2012; Nishida et al., 2013). Peltoniemi et al. have introduced a scattering model for small particles Peltoniemi et al. (2020), Peltoniemi (2007), Peltoniemi et al. (1989) that is recently extended to study laser momentum transfer to deflect dangerous objects to a safer course (Peltoniemi et al., 2021; Dumestier, 2021). In this work, we extend the model to wider range of space debris particles to support the observations.

Before productive use, the model must be validated. There is currently no way to measure real space debris particles in real conditions. The best we can do is to measure analogue particles in laboratory. This has limitations, but maps validity range. Laboratory gonioradiometers have been used to measure particle scattering behaviour, e.g. (Muinonen et al., 2019; Muñoz et al., 2010; Sasse et al., 1995; Bédard et al., 2014; Bédard et al., 2015). The Finnish Geospatial Research Institute (FGI) has long experience on field and laboratory goniometry Peltoniemi et al. (2014), Suomalainen et al. (2009), Kaasalainen et al. (2005), Näränen et al. (2004), Peltoniemi et al. (2021), Piironen et al. (1998). In this work, our measurements are done with a newly developed device and new samples.

3. Instrumentation: Masala space goniometer

The FGI space goniometer facility is a flexible system consisting of motors, arms, optics, and sensors. It can be easily configured for various scattering measurements. For the present experiment, a small self-standing system was built (Fig. 2) at FGI building in Masala. The base stands on wheels. On top is the azimuth motor on pillars. Over the azimuth motor is the turning frame, containing shelves for electronics, a base plate for the zenith motor, and a sample rotator. The zenith arm is fixed to the zenith motor. On the top end of the zenith arm is a cross arm, which contains the sensing optics oriented towards the centre of motion.

Currently the sensing optics includes a planoconvex BK7 lens of a diameter of 50 mm and a focal length of 75 mm. The lens is focused to infinity to avoid making an image of the target to the light fibre bundle input. Before the light cable input is a manual shutter. The optics are connected to the ASD FieldSpec 4 spectroradiometer by a 2 m long optical cable.

All motors are by Standa (8MR191-28, 8MR191-4247, and 8MR190-2–4247) with controllers (8SMC5-USB-B9-2). The controllers are connected to a Raspberry Pi 3 computer by a USB cable. The Raspberry Pi runs Linux and the control software is written in Python. Arbitrary measurement sequences can be created. Here, we chose 6 azimuth angles over the target, phase angle range $10° – 170°$, and 6 target orientations, as shown in Fig. 3. This sequence requires slightly over 1 h to complete. The data is written in a file for further processing and visualisation.
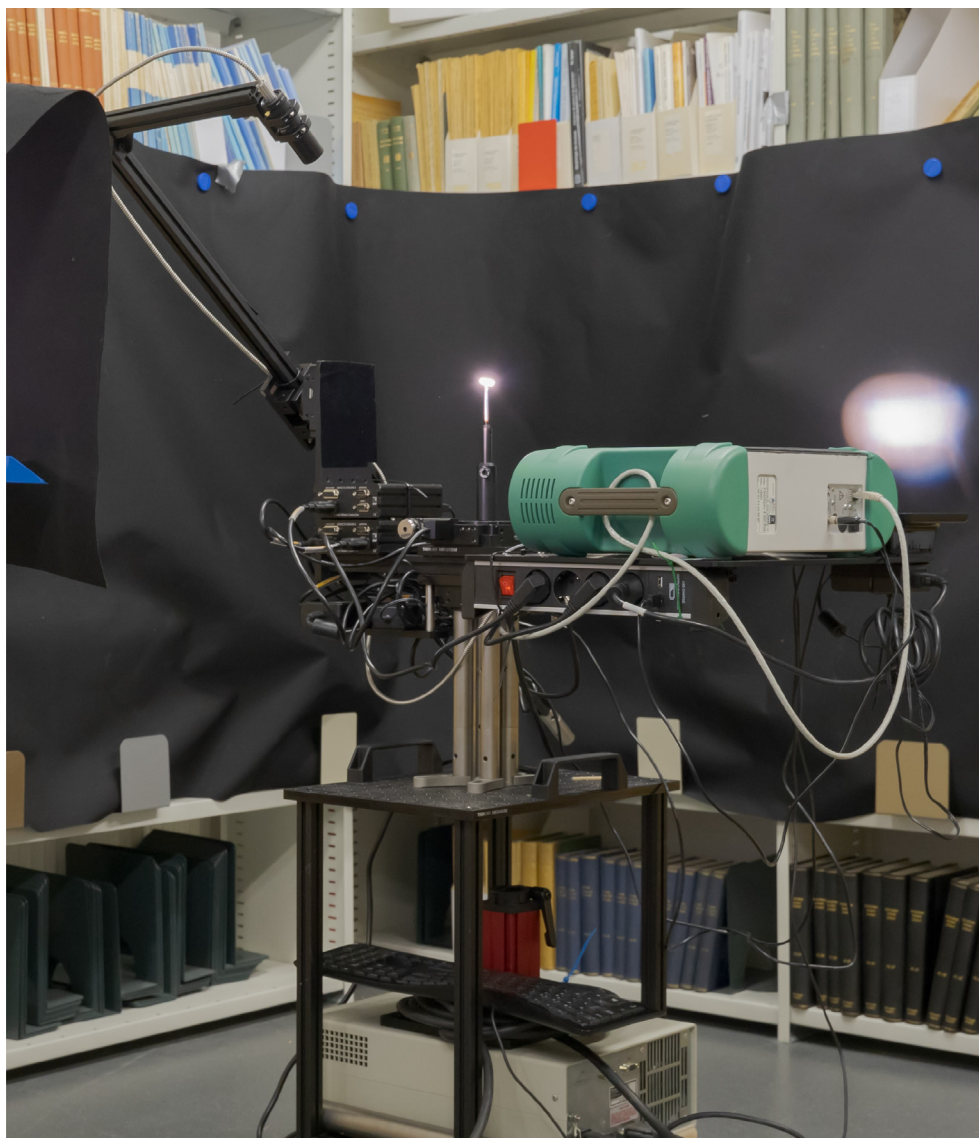
Fig. 2. FGI goniometer in a 2021 setup. The sample is the bright object in the middle. The green-gray box is ASD FieldSpec 4 spectroradiometer. The metal covered light cable connects the spectrometer body to the optics, on top of the black arm. The zenith motor is behind the black fabric left from the sample, and azimuth motors on top of the four pillars in the centre. Motor controllers are seen left to the spectroradiometer. The gray box on the bottom is the light source power controller. Light source itself is left from the image.

The light source is an Oriel QTH with 200 W of power. Two configurations were tried. In the first one, the light source stood on a separate table, and the light was collimated using a lens of 10 cm in diameter and focal length of 40 cm, to produce a beam of about 5 cm in diameter at the target. This gave strong and homogeneous, but a somewhat large spot. The problem was that the tighter focusing made light source filament structures visible. In the second configuration, the light source was standing inside the goniometer bottom frame. Light was focused into a liquid optical cable of a length of 2 m and a diameter of 5 mm. The other end of the cable was fixed horizontally 50 cm apart from the target. The light was focused on the target using a planoconvex lens of a diameter of 25 mm and focal length of 50 mm, which produces a homogeneous

spot of 2 cm in diameter at the target. The optical cable limits the measurement wavelengths to between 450 nm and 2000 nm, and causes some power losses, but the resulting tight focus compensates for these limitations. Both the light source and the sensing optics can be configured for polarisation measurements, but in here a non-polarising setup is used to collect maximal signal from a small target.

A small Spectralon (R) cylinder is used as a reference target (Fig. 4). Its absolute scattering properties are not characterised yet, but it gives a good reference for all targets.

The measurement sequence is as follows: turn power on, allow 30 min to warm the electronics and the light source. Measure dark current (D) and reference target (W). Start the target measurement, follow that goniometer arms move
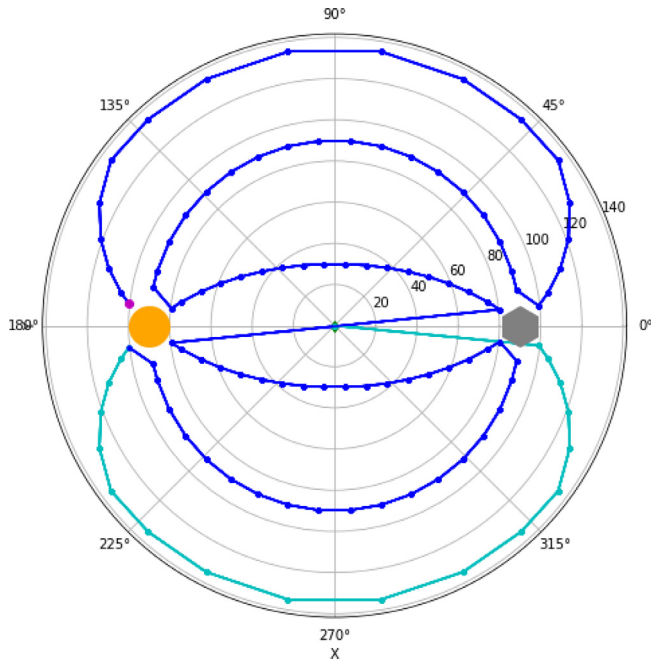
Fig. 3. The goniometer path in degrees. Cyan line shows the first sweep, continuing in blue, and ending with the red dot. Dots show the points where the measurements are taken. The orange circle on the left denotes the light source position (backward), and the gray hexagon on the right denotes the forward direction of the beam, both blocked from measurements.

fluently. After the measurements, measure again the reference for control and upload the data.

The scattering function S is computed as

$$S(\alpha, \phi, \iota, \xi) = \frac{T(\alpha, \phi, \iota, \xi) - D}{W(\alpha', \phi', \iota', \xi') - D}[S_W(\alpha', \phi', \iota', \xi')], \qquad (2)$$

where T is the measured signal from the target, D is the dark current, W is the signal from the reference, and primed quantities are the angles of the reference measurements. $[S_W]$ should be the known scattering function of the reference, but as we do not know it yet, we assume it to be unity and make only relative analysis here. If the target mount is causing interfering signal, we measure it separately and subtracted it from target as: $S' = S - S_{\mathrm{mount}}$.

The phase function P is approximated by normalising S:

$$P = \frac{4\pi S}{\int d\Omega S} \approx \frac{4\pi S}{\sum_i w_i S_i}, \qquad (3)$$

where the index i runs over the data points and w_i is an integration weight. Because the measurements did not cover all peaks, especially forward and backward and partially specular, and if covered the highest peaks saturated the sensor, the normalisation has some uncertainties.

The system has been unmounted in Masala and will be rebuilt in FGI new premises in Otaniemi, Espoo.

4. Samples

Fragments generated in four hypervelocity impact tests that were conducted at the Fraunhofer Institute for High-Speed Dynamics, Ernst-Mach-Institut, EMI in frame of the MIRAD study (Microparticle impact related attitude disturbances) Watson et al. (2020); Putzar et al. (2019) were used as samples. In the tests, spherical aluminium projectiles between 1.25 and 3.0 mm hit two types of targets: 10 mm thick monolithic CFRP (carbon fibre reinforced polymer) plate targets, and CFRP sandwich panels with an aluminium honeycomb core. Impact velocities were between 6.5 and 7.4 km/s. The tests generated
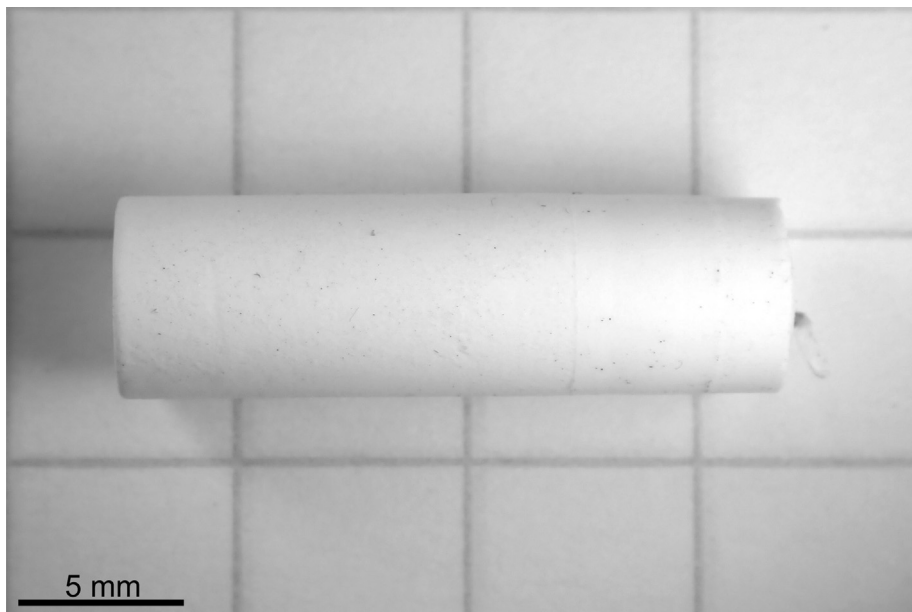

Fig. 4. A small Spectralon (R) cylinder used as an ad hoc reference. The scale bar on left bottom corner is 5 mm, and background cross-line distance is 7 mm.

both CFRP fragments and aluminium fragments (from the honeycomb cores). Most of the fragments generated are very small, below 0.1 mm.

We selected the two largest metal pieces for measurements, see Fig. 5. They originate from the honeycomb core and consist of Al 5056. The honeycomb core foil thickness was 25.4 µm and with perforations. The first metal sample is rather flat with ripples on the sides. The surface is partially shiny, but contains significant micrometer-scale roughness and dust adding diffuse reflection. The second metal piece is strongly bent with no preferred orientation. It can be surrounded by an ellipsoid of an aspect ratio about 1:2.

Most abundant material in the sample was CFRP. These were mostly in the form of long needles and a few flat flakes/plates. There were a few CFRP needles with a length of 1–2 cm that were selected for measurement, one CFRP plate of a few mm in its largest dimension (Fig. 6). The CFRP pieces consist of thin carbon fibre bundles inside epoxy. Each fibre has a diameter around 15 µm. The needles and flakes have both smooth and rough surfaces.

Further, for testing purposes, we measured pieces of iron wire, copper wire, and small paint flakes peeled off from a metal handrail.

We tried different techniques to mount the sample on the beam: thin black iron wire, spider webs, human hair, and a CFRP needle. First, the thin black iron wire worked well for the larger metal plate and paint flake, but for smaller particles it provided too large optical footprint. Next, the spider webs provided moderate footprint and allowed measuring smaller particles. However, handling the web is complicated, and the web is unstable, thus some uncertainty remains on how well the background is really subtracted. The spider shepherding was also considered challenging: they were not cooperative to make the web when needed and disappeared in the beginning of the winter season. Third, human hair was easier to handle and more stable than web but much thicker. Last, we sacrificed one thin CFRP needle as a holder and mounted some samples balancing on it. In all cases, we focused the light beam on the target as closely as possible to minimise any effect of mountings.

5. FGI space particle model

For particle sizes in the range 0.1–10 mm (or at least 100 times the longest measured wavelength), the geometrical optics domain is a sufficient approximation. Thus, we apply our ray-tracing technique for rough ellipsoids
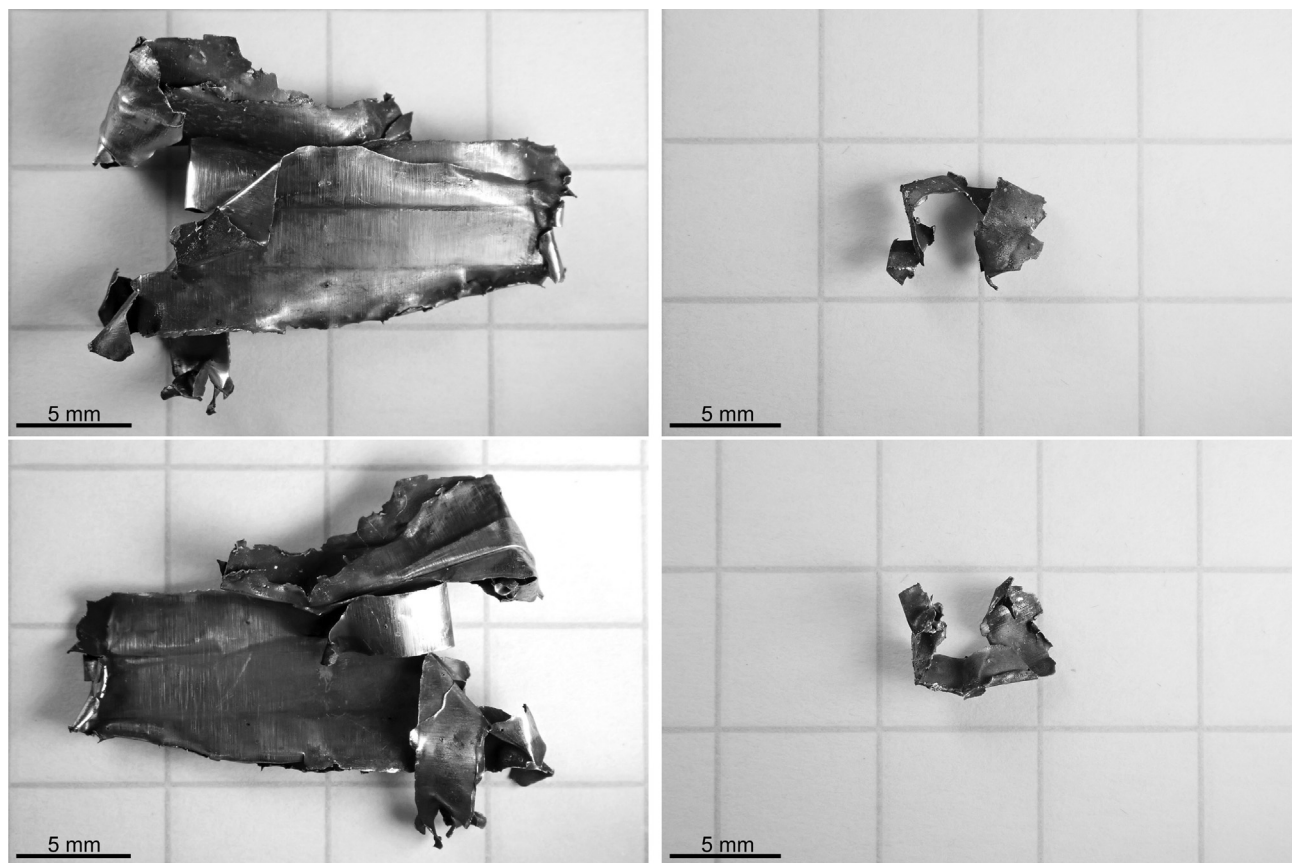

Fig. 5. Two metal samples used in measurements and analysis. The larger one is shown on the left, and the smaller one on the right, each one in two orientations. The scale bar on left bottom corner is 5 mm, and background cross-line distance is 7 mm.
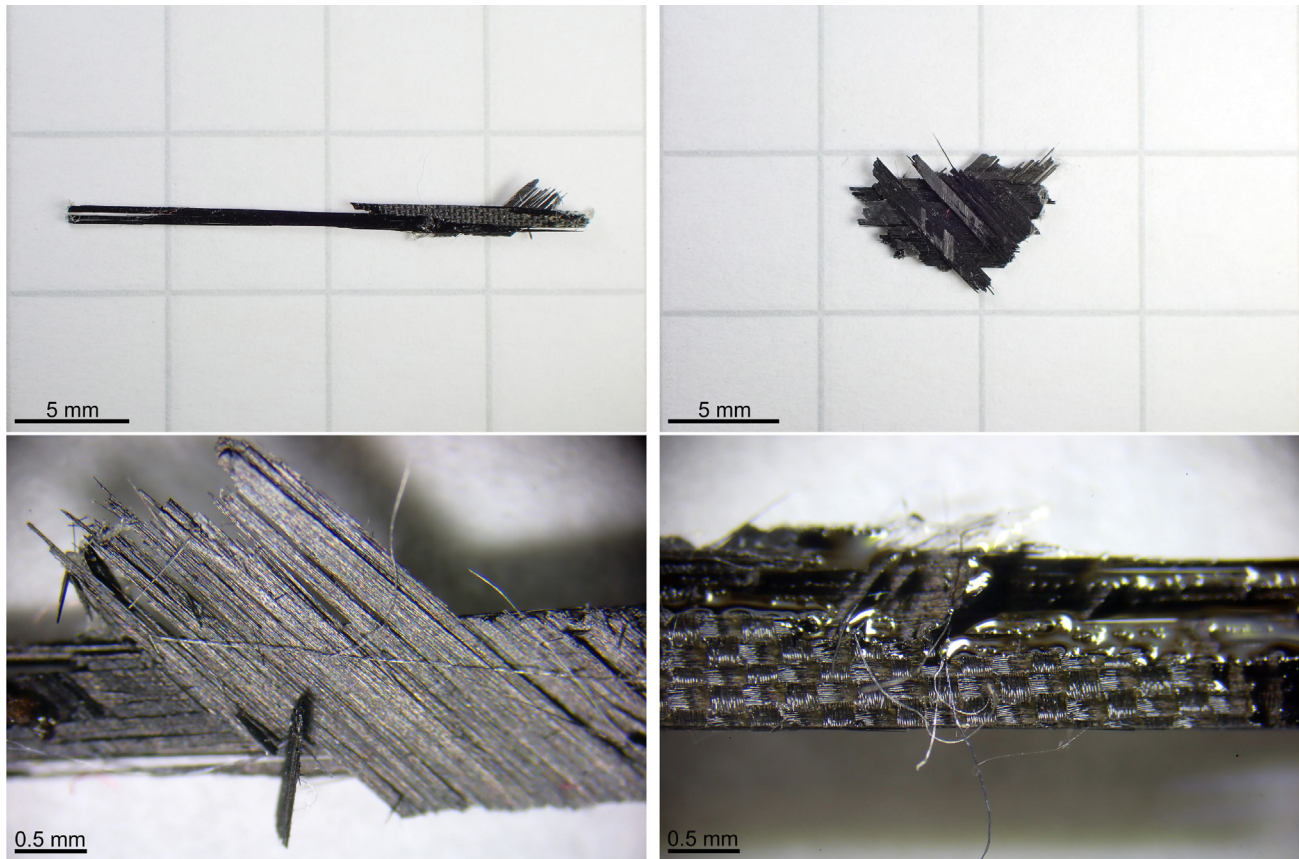
Fig. 6. Two CFRP samples: a needle (top left) and a flake (top right). The bottom panels show details of the needle at two different parts, such as bare carbon fibers and parts covered by epoxy, including both flat and rough surfaces. The black scale bar is 5 mm on the top images, and 0.5 mm on the bottom images.

Peltoniemi et al. (1989), Peltoniemi et al. (2020) complemented with two new elementary shapes (2 and 3 below):

1. ellipsoids, (aspect ratio 0.5 – 2),
2. capsuloids (elliptic spherocylinders, cylinder + hemispheres),
3. diskuloids (prolate spherocylinders, disk + hemitorus),
4. (cubic shapes under construction).

Each shape is parameterised by 3 main-axis-lengths. Further, the surface may have statistical deviation from mean shape, characterised by 2 statistical roughness parameters, one giving the standard deviation of radius/height, and the other the standard deviation of slope.

The optical properties are described by a complex refractive index, yielding Fresnel reflection and refraction coefficients for locally planar surfaces and absorption inside the sample. The refractive index values were searched from (Polyanskiy et al., 2022).

We further assume that there can be internal volume scatterers, *e.g.*, voids or other materials modelled with a scattering coefficient and phase function. Similarly, there can be small dust in a small layer on the surface. So far, we have computed the properties of the internal volume scatterers using a Monte Carlo volume-integral-equation technique with homogeneous random particlesPeltoniemi et al. (2020). Other methods are also possible but not evaluated here.

Table 2
The input variables used in the model computations presented in Figs. 7–11. "N el" is the number of elements, "semiaxis C" refers to outer size of the cluster in mm, and "semiaxis E" to the smallest element semi axis. "Volscat" means internal volume scatterers: "C" = carbon fibre needles of 10 μm in diameter, "Z" = ZnO rough spheres < 10 μm, or external: "D" = dust, and the numbers the scattering coefficient and albedo.

Fig.	Material	Shape	N el	Semiaxis C	Semiaxis E	Roughness	Volscat
7	CFRP	needle	1		0.1, 0.1, 1.0	0.1, 0.2	C, 1E4, 0.2
8	CFRP	flake	1		1.0, 1.0, 0.1	0.1, 0.2	C, 1E4, 0.2
9	Metal	bent	15	1.0, 1.0, 0.5	0.2, 0.2, 0.05	0.1, 1.1	-
10	Metal	bent	11	1.0, 1.0, 0.2	0.2, 0.2, 0.05	0.1, 0.3	D, 1E5, 0.2
11	Paint	flake	1		1.0, 1.0, 0.05	0.1, 0.3	Z, 1E5, 1.0

More complex particles are constructed by aggregating the elementary shapes together, overlapping, if necessary. We link our model to shapes used in SOCIT4 and DebriSat classes as follows:

- needle: long capsuloid, usually semi rough,
- flake: flat diskuloid, usually rough,
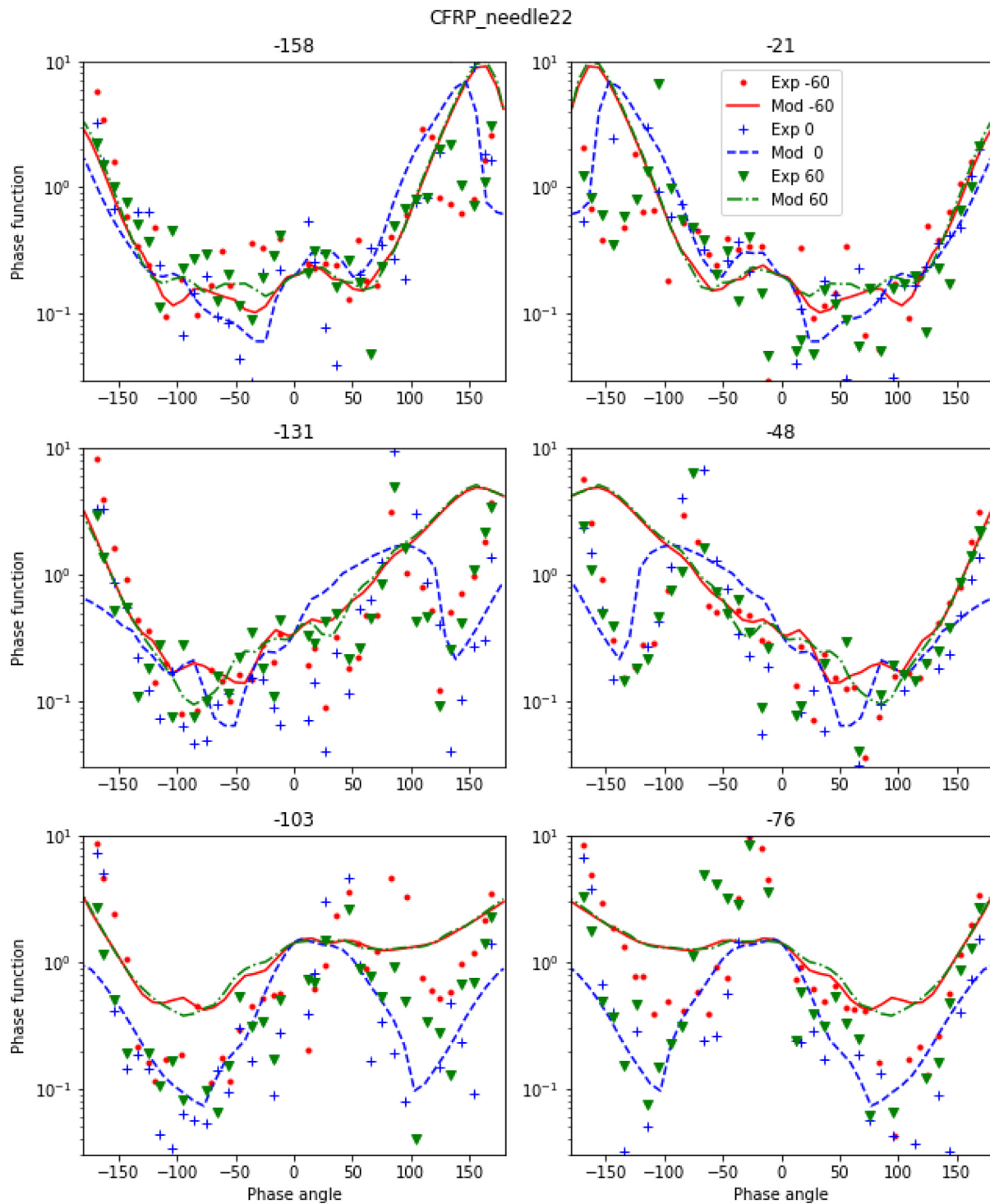- fibre: semi-smooth circular capsuloid,
- grain: rough ellipsoid,

Fig. 7. Measurement of the phase function (in 1/steradian) from the CFRP needle (symbols) compared to model (lines). The colours indicate three different azimuth directions ($0°, \pm 60°$). For clarity, $+180°$ azimuth angles are shown with negative phase angles. The target is rotated in six angles, shown in the titles, including front and back sides (left and right).
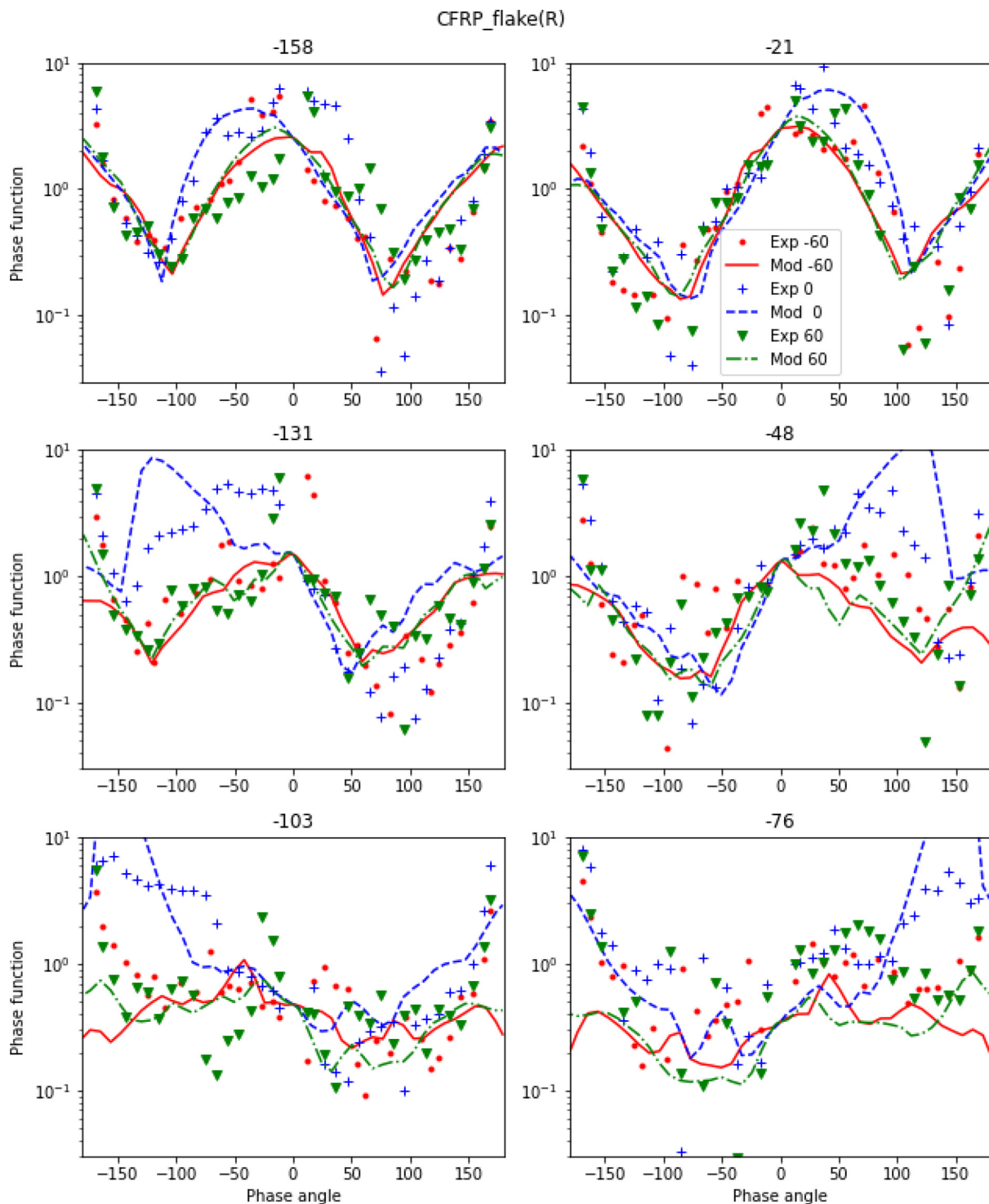
Fig. 8. Measurement from the CFRP flake compared to model, as in Fig. 7.

- droplet: smooth ellipsoid, almost sphere,
- bent plate: one central diskuloid, and few smaller ones around in random location and orientation, inside an ellipsoid, thicker or thinner,
- angled rod: joint capsuloids in angles,
- complex: an object formed by a mixture of different shapes.

6. Comparison of model and measurements

Below, we present a subset of the results obtained. For every measurement, a model example is shown. Model parameters are approximately fitted with a few iterations and are given in Table 2.

We plot for each particle the modelled and measured phase function in the 1050 ± 50 nm band, in 6 target orientations, and with 6 azimuth angles in Figs. 7–11.

The long CFRP needle shows strong dependence on the tilt angle, and clear specular effect from planar surface (Fig. 7). The scattering can be very low along the long axis,

as expected. Transmission is weak or close to none. Model agrees reasonable well, except near backscattering in a number of cases.

The visible profile determines also well the scattering from a CFRP flake (Fig. 8). Model can predict well the major scattering feature, though the brightness maximum
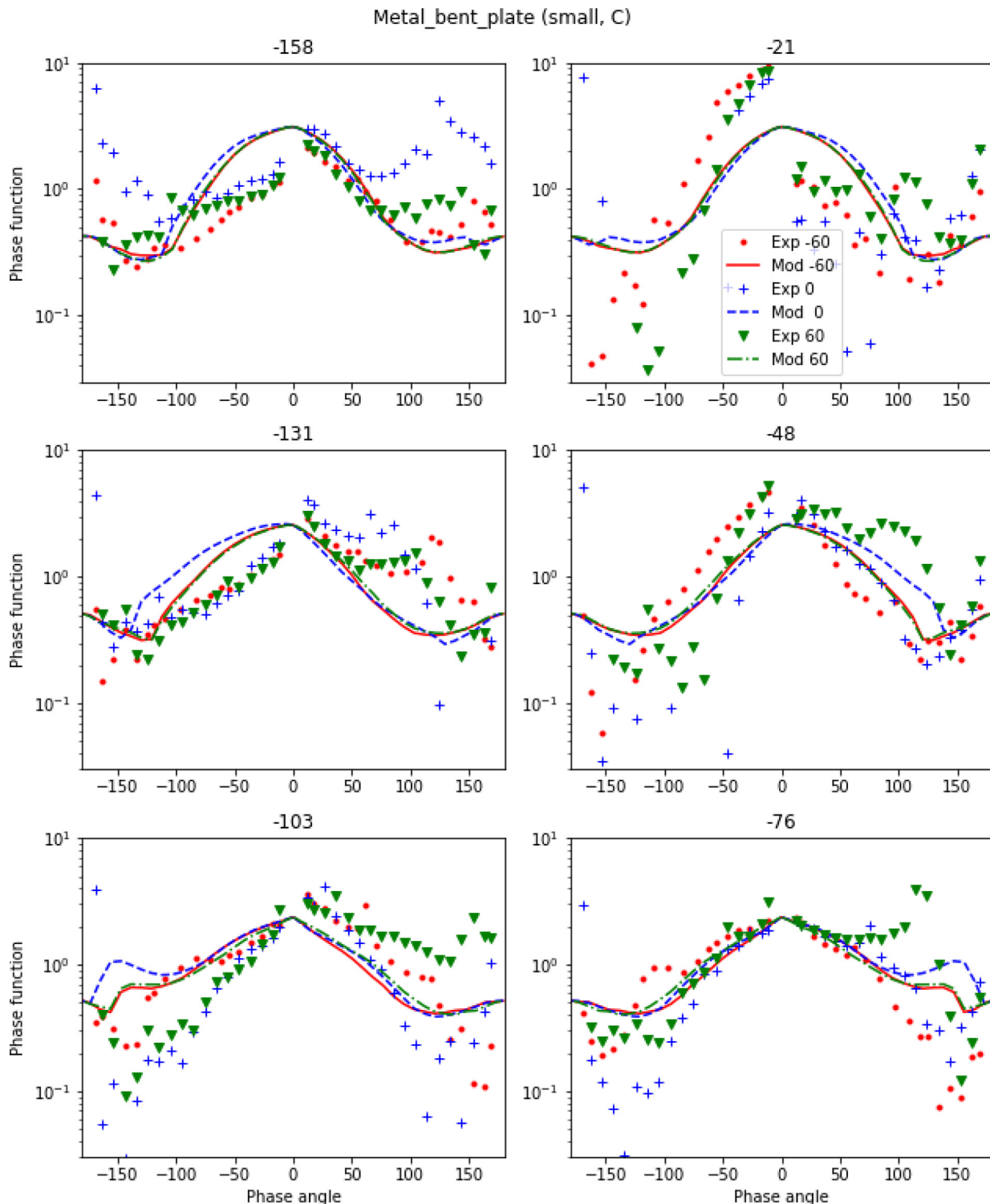

Fig. 9. Smaller metal plate, as in Fig. 7.
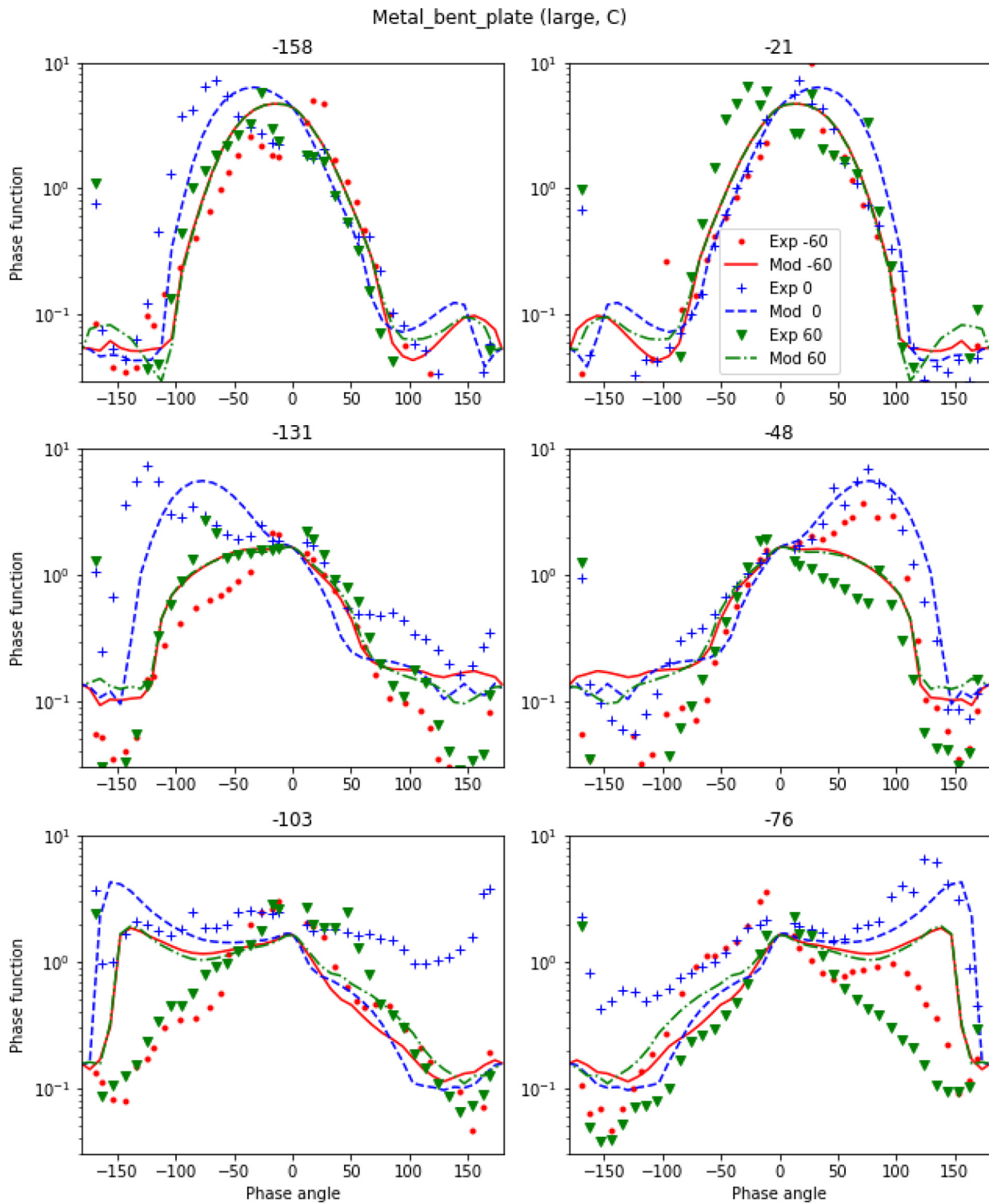
Metal_bent_plate (large, C)

Fig. 10. Larger metal plate, as in Fig. 7.

is sometimes shifted. Model may be improved by treating the bare fibers and epoxy in more detail.

The smaller metal plate has many irregularities (Fig. 9). It has some non-systematic orientation dependence. The particle is modelled as an ellipsoidal cluster of randomly oriented plates, with moderate roughness and small amount of dust

on the surface. The first plate is triple sized compared to the rest, and is in fixed orientation in the centre, aligned with the cluster shape. Overall scattering is well predicted, though back-scattering may need more fine tuning.

The larger metal plate is more planar than the small one (Fig. 10). There is a peak in the specular direction,
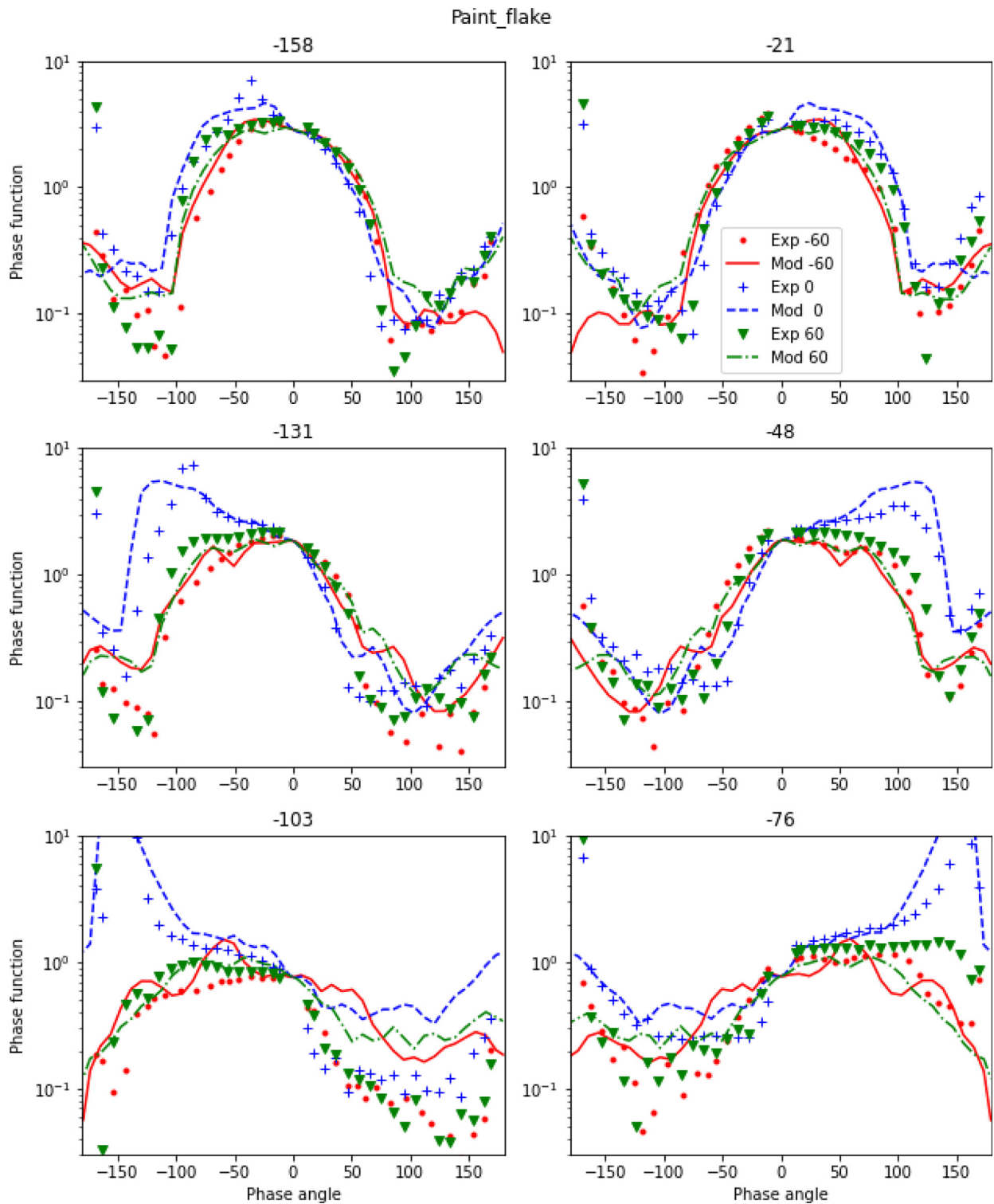
Fig. 11. A small paint flake taken from a hand rail outside FGI, as in Fig. 7.

although rather wide, due to multiply bent surface. Again, the particle is modelled as one central plate in fixed orientation and 10 smaller plates in random orientation, with small amount of dust, and moderate surface roughness. As with smaller metal grain, the overall scat-

tering is well predicted, but back-scattering needs fine tuning.

Paint flake agrees with the model in an excellent way (Fig. 11). Although the two sides were of visually different colour, their phase functions behave similarly.
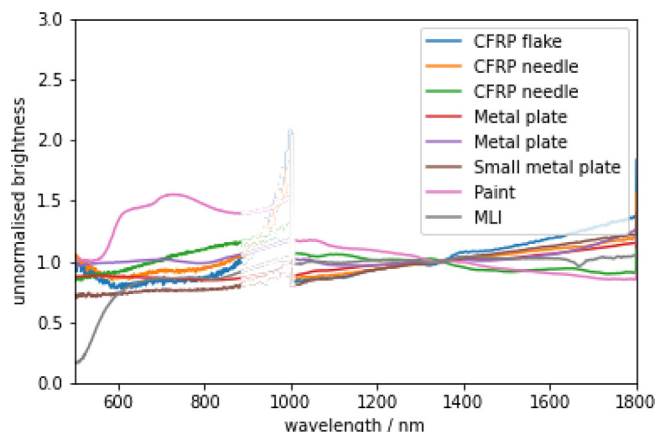
Fig. 12. The scattered spectrum, relative to the white reference of the samples: 3 * CFRP, 2 * metal, paint, and MLI. The spectrometer had a hardware failure in NVIS channel dark current measures, thus most infected parts are washed out.

Finally, we compare the spectra of the measured samples in Fig. 12. The spectra are averaged over all orientations and the phase angle range of 10°–45°, that is probably typical observation range in the COLA experiment, but skips the back-scattering where sensors are partially saturated. The spectra are arbitrarily normalised to 1 at 1350 nm. The signal is very low in some wavelengths, thus only the best part of the range is shown. Otherwise, the differences between metallic and CFRP samples are not too clear based on the few samples and deviations between same class samples. Paint of course differs, as it had a colour, though real space paints may have any other colour. For comparison, a multi layer insulation (MLI) sample from the Olamot (in Orbit Laser Momentum Transfer) project (Peltoniemi et al., 2021) is also shown, and it has a clear signature below 500 nm. However, MLI pieces are assumed to be rather rare below 1 cm range by MASTER.

7. Analysis

In general, the model agrees with the measurement fairly well. There are sure many disagreements in details, but a simple model cannot produce all features of complicated particle shapes. The differences between targets are reproduced well to separate them. There can be at least ±10° uncertainty in target rotation angles, because the mounting was not very stable. Thus, small shifts in specular direction are not worrying. As the measured samples were just random choices of an irregular ensemble, it is not productive to make detailed model fits and statistical analyses with just these cases, but rather look at the overall behaviour.

Metallic particles remain opaque in the size range, and show no size signatures. The paint piece was also opaque. The smallest plastic and CFRP pieces are already transforming slightly transparent around 0.1 mm, but it can still be difficult to do sizing by phase curves. Brightness depends

of course directly on the size, but there remains about a factor of 10 uncertainty.

Flat, round, and long particles have clear azimuthal signatures. Flat particles scatter most anisotropically towards the flat side, needles more cylindrically, and round more isotropically. The shape signal mixes with orientation. Rough surfaces produce more backscattering than smooth ones.

Material estimates can probably be obtained only indirectly. The measured and modelled objects showed quite weak spectral signatures, and artificial colouring can cause arbitrary effects. The phase function depends on the shape and orientation more than on the material. The variations within the same material class also seem to be rather large compared to the differences between classes.

8. Conclusions

We have developed an empirical light-scattering model for sub-cm space-debris particles based on measurements using a novel laboratory setup. The model agrees with the measurement data satisfactory. Most work remaining concerns modelling near forward and backward scattering directions, but because the measurements are also most uncertain there, we must leave more detailed studies for the future. Of course, every particle is unique, and thus fit for real space-debris particles is at best statistical.

The measurement setup was found flexible and productive, although compromised by original purpose for much larger objects. Making beam just the size of the target, and sensor field of view somewhat larger produced the best results. Problems still exist in saturation handling, small phase angles ($< 10°$), large phase angles ($> 170°$), spectrum calibration, and sensitivity. All these could be improved with rather moderate costs and efforts. Using lasers and optimal sensors would give more range and sensitivity.

The mounting of small targets posed a challenge. Largest objects could be mounted using needles, but with smaller objects, the needle is as bright as the target, occasionally even brighter. Thus, even when subtracting the bare needle, much uncertainty remains. Spider web construction provided much smaller footprint, but just when we got the measurement process smooth, the spiders vanished, and new stock is not available in winter. Hair was somewhere between the needle and web. Stable levitation system could be tried next.

The biggest challenge is the large variability of the targets. Even the simplest ones are asymmetric in all directions, and contain randomly rough and smooth surfaces. Dark dielectric particles (plastics, minerals) are just in the domain where a small size variation can turn opaque particles transparent or vice versa. Much more measurements and more detailed characterisation of particle properties, including size, shape, material, internal scatterer structure, are still needed. Largest space particle class missed here is the small paint flakes of real space paint, followed by metal needles, and objects composed of a mixture of different

shapes. There is also a need to handle smaller particles. In the future, meteorite fragments can be studied using the same instrumentation and modelling.

For operational data interpretation, this work suggests that quite a good range of phase and azimuth angles are needed. From coaxial setup one can probably distinguish crushed metal by strong back-scattering and needles and paints by a flatter, asymmetric curve. More azimuth angles may help identifying needles.

Declaration of Competing Interest

The authors declare that they have no known competing financial interests or personal relationships that could have appeared to influence the work reported in this paper.

Acknowledgements

References

Abbasi, V., Thorsteinson, S.. Balam, D., Rowe, J., Laurin, D., Scott, R.L., Doyon, M., 2019. The NEOSSat Experience: 5 years in the life of Canada's space surveillance telescope, https://conference.sdo.esoc.esa.int/proceedings/neosst1/paper/494.

Akahoshi, Y., Faure, P., Matsumoto, H., Kitazawa, Y., 2012. Hypervelocity Impact Tests on Ejecta and its International Stabdarization. J. Space Technol. Sci. 26 (2), 2_48–2_55. https://doi.org/10.11230/jsts.26.2_48.

Allen, S., Fitz-Coy, N., 2020. DebriSat fragment characterization: Quality assurance. J. Space Saf. Eng. 7 (3), 235–241. https://doi.org/10.1016/j.jsse.2020.08.001, URL https://www.sciencedirect.com/science/article/pii/S2468896720300987.

Bédard, D., Lévesque, M., 2014. Analysis of the CanX-1 Engineering Model Spectral Reflectance Measurements. J. Spacecraft Rock. 51 (5), 1492–1504. https://doi.org/10.2514/1.A32643, https://arc.aiaa.org/doi/10.2514/1.A32643.

Bédard, D., Wade, G., Abercromby, K., 2015. Laboratory Characterization of Homogeneous Spacecraft Materials. J. Spacecraft Rock. 52, 1–19. https://doi.org/10.2514/1.A33079.

Bohren, G.F., Huffman, D.R., 1983. Absorption and Scattering of Light by Small particles. John Wiley & Sons, New York.

Bouquet, A., Baratoux, D., Vaubaillon, J., Gritsevich, M.I., Mimoun, D., Mousis, O., Bouley, S., 2014. Simulation of the capabilities of an orbiter for monitoring the entry of interplanetary matter into the terrestrial atmosphere. Planet. Space Sci. 103, 238–249. https://doi.org/10.1016/j.pss.2014.09.001, URL https://www.sciencedirect.com/science/article/pii/S0032063314002785.

Cowardin, H., Anz-Meador, P., Murray, J., Liou, J.-C., Christiansen, E., Sorge, M., Fitz-Coy, N., Huynh, T., 2020. Updates to the DebriSat Project in Support of Improving Breakup Models and Orbital Debris Risk Assessments, American Society of Mechanical Engineers Digital Collection, https://doi.org/10.1115/HVIS2019-066. URL https://asmedigitalcollection.asme.org/hvis/proceedings/HVIS2019/883556/V001T10A012/1085253.

DISCOS, https://discosweb.esoc.esa.int/.

Dumestier, D., 2021. Space Debris Deflection by Space Based Laser. In: 8th European Conference on Space Debris. URL https://conference.sdo.esoc.esa.int/proceedings/sdc8/paper/180.

Englert, C.R., Bays, J.T., Marr, K.D., Brown, C.M., Nicholas, A.C., Finne, T.T., 2014. Optical orbital debris spotter. Acta Astronaut. 104 (1), 99–105. https://doi.org/10.1016/j.actaastro.2014.07.031, URL https://www.sciencedirect.com/science/article/pii/S0094576514002872.

ESA, Space Debris Office, ESA's Space Environment Report 2022. URL https://www.esa.int/Safety_Security/Space_Debris/ESA_s_Space_Environment_Report_2022.

Flegel, S., Gelhaus, J., Wiedemann, C., Vörsmann, P., Oswald, M., Stabroth, S., Klinkrad, H., Krag, H., 2009. The MASTER-2009 space debris environement model, European Space Agency, (Special Publication) ESA SP 672.

Flegel, S., Gelhaus, J., Wiedemann, C., Vörsmann, P., Oswald, M., Stabroth, S., Klinkrad, H., Krag, H., 2009. The MASTER-2009 space debris environement model. European Space Agency, (Special Publication) ESA SP 672.

Flohrer, T., Lemmens, S., Bastida Virgili B., Krag, H., Klinkrad, H., Parrilla, E., Sanchez, N., Oliveira, J., Pina, F., 2013. DISCOS- Current Status and Future Developments. URL https://conference.sdo.esoc.esa.int/proceedings/sdc6/paper/163.

Fragmentation database, https://fragmentation.esoc.esa.int/home.

Helander, P., Puranen, T., Meriläinen, A., Maconi, G., Penttilä, A., Gritsevich, M., Kassamakov, I., Salmi, A., Muinonen, K., Hæggström, E., 2020. Omnidirectional microscopy by ultrasonic sample control. Appl. Phys. Lett. 116 (19), 194101. https://doi.org/10.1063/5.0002602, https://aip.scitation.org/doi/10.1063/5.0002602.

Kaasalainen, S., Peltoniemi, J., Näränen, J., Suomalainen, J., Kaasalainen, M., Stenman, F., 2005. Small-angle goniometry for backscattering measurements in the broadband spectrum. Appl. Opt. 44 (8), 1485–1490.

Krisko, P.H., Horstman, M., Fudge, M.L., 2008. SOCIT4 collisional-breakup test data analysis: With shape and materials characterization. Adv. Space Res. 41 (7), 1138–1146. https://doi.org/10.1016/j.asr.2007.10.023, URL http://www.sciencedirect.com/science/article/pii/S0273117707010423.

Krisko, P.H., Flegel, S., Matney, M.J., Jarkey, D.R., Braun, V., 2015. ORDEM 3.0 and MASTER-2009 modeled debris population comparison. Acta Astronaut. 113, 204–211. https://doi.org/10.1016/j.actaastro.2015.03.024, URL https://www.sciencedirect.com/science/article/pii/S0094576515001241.

Laurin, D., Hildebrand, A., Cardinal, R., Harvey, W., Tafazoli, S., 2008. NEOSSat: a Canadian small space telescope for near Earth asteroid detection. In: Space Telescopes and Instrumentation 2008: Optical, Infrared, and Millimeter, vol. 7010, SPIE, pp. 343–354. https://doi.org/10.1117/12.789736. https://www.spiedigitallibrary.org/conference-proceedings-of-spie/7010/701013/NEOSSat-a-Canadian-small-space-telescope-for-near-Earth/10.1117/12.789736.full.

Maconi, G., Penttilä, A., Kassamakov, I., Gritsevich, M., Helander, P., Puranen, T., Salmi, A., Hæggström, E., Muinonen, K., 2018. Non-destructive controlled single-particle light scattering measurement. J. Quant. Spectrosc. Radiat. Transfer 204, 159–164. https://doi.org/10.1016/j.jqsrt.2017.09.005.

Maconi, G., Helander, P., Gritsevich, M., Salmi, A., Penttilä, A., Kassamakov, I., Hæggström, E., Muinonen, K., 2020. 4pi Scatterometer: A new technique for understanding the general and complete scattering properties of particulate media. J. Quant. Spectrosc. Radiat. Transfer 246, 106910. https://doi.org/10.1016/j.jqsrt.2020.106910, URL http://www.sciencedirect.com/science/article/pii/S0022407319306776.

MASTER, https://sdup.esoc.esa.int/master/.

Mishchenko, M., Hovenier, J., Travis, L. (Eds.), 2000. Light Scattering by Non-Sperical Particles: Theory, Measurements and Applications. Academic Press, San Diego.

Muinonen, K., Vaisanen, T., Martikainen, J., Markkanen, J., Penttila, A., Gritsevich, M., Peltoniemi, J., Blum, J., Herranen, J., Videen, G., Maconi, G., Helander, P., Salmi, A., Kassamakov, I., Haeggstrom, E., 2019. Scattering And Absorption of Light in Planetary Regoliths. J. Vis. Exp. 149, e59607. https://doi.org/10.3791/59607.

Muñoz, O., Moreno, F., Guirado, D., Ramos, J.L., López, A., Girela, F., Jerónimo, J.M., Costillo, L.P., Bustamante, I., 2010. Experimental determination of scattering matrices of dust particles at visible wavelengths: The IAA light scattering apparatus. JQSRT 111 (1), 187–196.

Näränen, J., Kaasalainen, S., Peltoniemi, J., Heikkilä, S., Granvik, M., Saarinen, V., 2004. Laboratory photometry of planetary regolith analogs. II. Surface roughness and extremes of packing density. Astron. Astrophys. 426, 1103–1109.

Nishida, M., Kato, H., Hayashi, K., Higashide, M., 2013. Ejecta Size Distribution Resulting from Hypervelocity Impact of Spherical Projectiles on CFRP Laminates. Procedia Eng. 58, 533–542. https://doi.org/10.1016/j.proeng.2013.05.061, URL https://www.sciencedirect.com/science/article/pii/S1877705813009673.

Pardini, C., Anselmo, L., 2011. Physical properties and long-term evolution of the debris clouds produced by two catastrophic collisions in earth orbit. Adv. Space Res. 48 (3), 557–569. https://doi.org/10.1016/j.asr.2011.04.006, URL http://www.sciencedirect.com/science/article/pii/S0273117711002432.

Peltoniemi, J.I., 2007. Spectropolarised ray-tracing simulations in densely packed particulate medium. J. Quant. Spectrosc. Radiat. Transfer 108 (2), 180–196.

Peltoniemi, J.I., Lumme, K., Muinonen, K., Irvine, W.M., 1989. Scattering of Light by Stochastically Rough Particles. Appl. Opt. 28 (19), 4088–4095.

Peltoniemi, J.I., Hakala, T., Suomalainen, J., Honkavaara, E., Markelin, L., Gritsevich, M., Eskelinen, J., Jaanson, P., Ikonen, E., 2014. A detailed study for the provision of measurement uncertainty and traceability for goniospectrometers. J. Quant. Spectrosc. Radiat. Transfer 146, 376–390.

Peltoniemi, J.I., Gritsevich, M., Markkanen, J., Hakala, T., Suomalainen, J., Zubko, N., Wilkman, O., Muinonen, K., 2020. A Composite Model for Reflectance and Polarisation of Light from Granulate Materials. ISPRS Ann. Photogram. Remote Sens. Spatial Informat. Sci. V-1-2020, 375–382. https://doi.org/10.5194/isprs-annals-V-1-2020-375-2020, URL https://www.isprs-ann-photogramm-remote-sens-spatial-inf-sci.net/V-1-2020/375/2020/.

Peltoniemi, J., Gritsevich, M., Moilanen, J., Mitev, V., Roulet, J.C., Millinger, M., 2021. In-Orbit Coincident Lasersheet Particle Monitor, 84, 6188, Conference Name: 84th Annual Meeting of the Meteoritical Society ADS Bibcode: 2021LPICo2609.6188P. https://ui.adsabs.harvard.edu/abs/2021LPICo2609.6188P.

Peltoniemi, J.I., Wilkman, O., Gritsevich, M., Poutanen, M., Raja-Halli, A., Näränen, J., Flohrer, T., Di Mira, A., 2021. Steering reflective space debris using polarised lasers. Adv. Space Res. 67 (6), 1721–1732. https://doi.org/10.1016/j.asr.2021.01.002, URL https://www.sciencedirect.com/science/article/pii/S0273117721000211.

Piironen, J., Muinonen, K., Nousiainen, T., Sasse, C., Roth, S., Peltoniemi, J., 1998. Albedo measurements on meteorite particles. Planet. Space Sci. 46 (8), 937–934.

Polyanskiy, M.N., 2022. Refractive index database, https://refractiveindex.info, accessed on 2022-02-18.

Putzar, R., Watson, E., Schimmerohn, M., Kärräng, P., Millinger, M., 2019. How hypervelocity impacts can affect the LISA mission -The MIRAD study. In: 70th International Astronautical Congress 2019At: Washington, D.C., USA.

Sasse, C., Peltoniemi, J.I., 1995. Angular scattering measurements and calculations of rough spherically shaped carbon particles. In: Proc. SPIE 2541, Optical Scattering in the Optics, Semiconductor, and Computer Disk Industries, no. 131, https://doi.org/10.1117/12.218329.

Schimmerohn, M., Matura, P., Cardone, T., de Wilde, D., Krag, H., 2018. Numerical simulations for spacecraft catastrophic disruption analysis. In: Clean Space Industrial Days 2018, URL https://indico.esa.int/event/234/contributions/3927/.

Suomalainen, J., Hakala, T., Peltoniemi, J., Puttonen, E., 2009. Polarised Multiangular Reflectance Measurements Using Finnish Geodetic Institute Field Goniospectrometer. Sensors 9 (5), 3891–3907. https://doi.org/10.3390/s90503891.

Torre, C., Pina Caballero, F., Sánchez-Ortiz, N., Sdunnus, H., Klinkrad, H., 2011. DISCOS database and web interface. In: Proceedings of the Third European Conference on Space Debris, 19–21 March 2001, Darmstadt, Germany. 2 (ESA SP-473).

van de Hulst, H.C., 1957. Light Scattering by Small Particles. John Wiley & Sons, New York.

Watson, E., Kunert, N., Putzar, R., Maas, H.-G., Hiermaier, S., 2020. Four-view split-image fragment tracking in hypervelocity impact experiments. Int. J. Impact Eng 135, 103405. https://doi.org/10.1016/j.ijimpeng.2019.103405, URL https://www.sciencedirect.com/science/article/pii/S0734743X19308024.

Worms, J.C., Girard, O., Hauchecorne, A., Muinonen, K., 1999. LIBRIS: An orbital imaging lidar for the detection of small to medium-sized debris in low-earth orbit. Adv. Space Res. 23 (1), 67–70. https://doi.org/10.1016/S0273-1177(98)00231-2, URL https://www.sciencedirect.com/science/article/pii/S0273117798002312.